Gate-defined quantum point contact in an InSb two-dimensional electron gas

Zijin Lei ●,* Christian A. Lehner ●, Erik Cheah, Christopher Mittag, Matija Karalic, Werner Wegscheider,
Klaus Ensslin ●, and Thomas Ihn ●

Solid State Physics Laboratory, ETH Zurich, CH-8093 Zurich, Switzerland

We investigate an electrostatically defined quantum point contact (QPC) in a high-mobility InSb two-dimensional electron gas. Well-defined conductance plateaus are observed, and the subband structure of the QPC is extracted from finite-bias measurements. The Zeeman splitting is measured in both in-plane and out-of-plane magnetic fields. We find an in-plane g factor $|g_\parallel^*| \approx 40$. The out-of-plane g factor is measured to be $|g_\perp^*| \approx 50$, which is close to the g factor in the bulk.

Indium antimonide (InSb) is a III-V binary compound known for its low effective mass, giant effective g factor in the bulk, and its large spin-orbit interactions (SOIs) [1–5]. These unique properties are interesting in view of applications such as high-frequency electronics [6], optoelectronics [7], and spintronics [8]. Recently, InSb, as well as InAs, has received more and more attention as a candidate to realize Majorana zero modes at the boundary to topological superconductors [9]. The topological superconducting phase can be achieved by combining superconductivity induced by proximity effects, control of the Zeeman field, a strong Rashba SOI, and the phase of Josephson junctions or superconducting quantum interference devices if the system is two (2D) or three dimensional (3D) [9–13]. An in-depth understanding of InSb nanostructures is necessary for scaling up and integrating potential InSb-based topological quantum devices. Investigating the Zeeman effect and SOIs at the nanoscale will help us to understand the topological nontrivial phase achieved in Majorana nanodevices. A quantum point contact (QPC) is one of the basic nanostructures, where a ballistic charged-carriers system is confined into a one-dimensional (1D) channel. In such a structure, the conductance of the channel is quantized in integer multiples of the conductance quantum e^2/h [14–16]. Therefore, the conductance e^2/h is called conductance quantum as a natural unit. Conductance quantization has been found in InSb nanostructures based on as-grown nanowires [17–20], nano sails [21], and other freestanding nanomaterials [22,23]. However, reports on InSb QPCs defined in InSb quantum wells (QWs) are still rare. Conductance quantization in InSb QWs is difficult to achieve [24–27], even though high-mobility InSb QWs can nowadays be grown with molecular beam epitaxy (MBE) [28,29], and various transport experiments have been performed [30–34]. While carrier mobility is high (several $100\,000\,\mathrm{cm}^2/\mathrm{Vs}$) and therefore the elastic mean free path easily exceeds the dimensions of the QPCs, time-dependent shifts of the device characteristics lead to serious hysteresis effects when sweeping the gate voltages. This is the main obstacle for high-quality InSb-QW-based QPCs and other nanostructures such as quantum dots. Due to this time-dependent effect, it is challenging to deplete the 2D electron gas (2DEG) in the QW in a stable way for a sufficiently long period of time, during which a transport experiment can be performed. The reason for the time-dependent effect may be related to the Si doping in the InAlSb barriers, from which the electrons in the QWs originate [35]. In previous papers, a chemical etching method was adopted to define a 1D channel, and a metal top gate or a pair of side gates were used to tune the density in the channel locally to achieve a stable pinch-off [26,27]. As a comparison provided in the Supplementary Material of Ref. [26], a gate-defined QPC in an InSb QW was characterized to be inferior in quality. The etching method seriously limits the device quality due to the induced scattering centers at the edges of the fabricated structures. Furthermore, the etching step makes the design and processing of integrated nanodevices much more challenging than gate-defined devices. Recently, Kulesh *et al.* [35] reported a purely gate-defined stable quantum dot on InSb QWs. To solve the problem of hysteresis, an undoped InSb QW was used, and an extra global top gate was added to induce electrons into the QW electrostatically. This undoped InSb may have higher mobility due to the absence of the remote ionized scattering centers. Nevertheless, the potential of this kind of QWs still needs to be investigated in further experiments.

In this paper, we study a QPC defined electrostatically in an InSb 2DEG populated by remote doping. We provide a detailed characterization of its energy levels, magnetoelectric subband structure, and effective g factor with the magnetic field applied in different directions relative to the plane of the 2DEG. With a special procedure for sweeping the gate voltage, the QPC can be dynamically stabilized, enabling successive measurements with nearly identical electronic conditions.

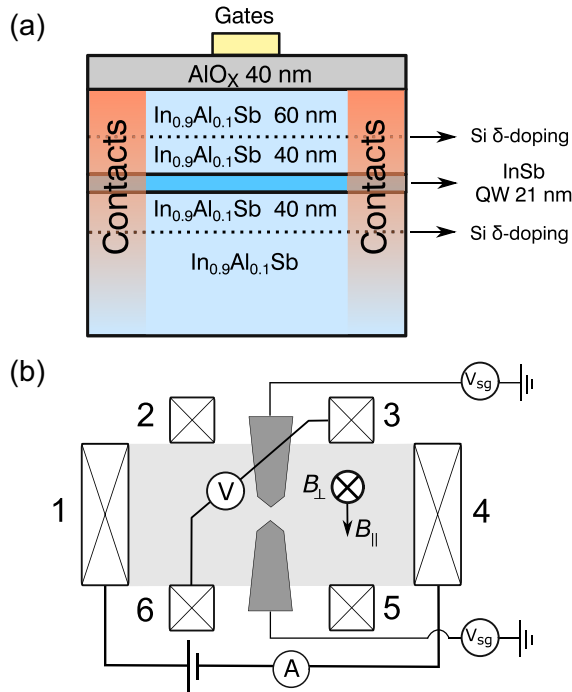*Corresponding author: zilei@phys.ethz.ch

FIG. 1. (a) Layer structure of the quantum well (QW) heterostructure. (b) A schematic representation of the quantum point contact (QPC). The QPC is defined on a standard Hall bar geometry (light gray). The gates of the QPC (dark gray) are evaporated on the ALOx dielectric layer. The gates separation is 200 nm. The in-plane and out-of-plane magnetic field $B_\parallel$ and $B_\perp$ are defined as illustrated. The current and voltage are measured in the configuration presented here as well.

Figure 1(a) shows the layer sequence of the sample. The InSb QW containing the 2DEG on which the QPC is defined is grown on a (100) GaAs substrate by MBE. An interfacial misfit transition to the GaSb buffer and an interlayer InAlSb buffer is employed to overcome the lattice mismatch between GaAs and InSb. The total thickness of the buffer layers amounts to roughly $3\,\mu$m. The 21 nm thick InSb QW is surrounded by $In_{0.9}Al_{0.1}Sb$ confinement barriers, the n-type carriers are introduced to the QW by two Si δ-doping layers incorporated in the barriers, 40 nm below and above the QW, respectively. On the top of the QW, an $In_{0.9}Al_{0.1}Sb$ layer with a thickness of 100 nm is grown. More details about the MBE growth can be found in Ref. [29].

Figure 1(b) shows a schematic diagram of the QPC gate structure and the measurement setup. The QPC here is defined on a standard Hall bar structure (light gray in the figure). The fabrication process of the Hall bar is like in our previous paper [34]. First, a Hall bar structure with the size of $400 \times 200\,\mu$m^2 is defined by wet chemical etching with an etching depth of more than 160 nm, which is deeper than the Si δ-doping layer on the substrate side. Second, layers of Ge/Ni/Au are evaporated onto the contact areas after Ar milling. In the next step, the sample is coated with a 40 nm thick aluminum oxide (ALO) dielectric layer using atomic layer deposition (ALD) at a temperature of 150 °C. A high-temperature annealing step is unnecessary because the metal diffuses into the material during the ALD process, which heats

the sample. Finally, pairs of split gates are deposited onto the ALO layer. To avoid a potential interruption of the gates of the gate-metallization at the mesa edge, we first fabricate the inner thin (5/25 nm) Ti/Au nanometer-sized gates (dark gray in the figure) on top of the mesa with standard electron beam lithography followed by electron beam evaporation. Then we use optical lithography and electron beam evaporation to define the thick (10/120 nm) Ti/Au micrometer-sized gate patches to connect the fine gates across the mesa edge to contact pads outside the mesa structure. The QPC measured in this paper has a split-gate separation of 200 nm. Before further studying the QPC, we characterize the 2DEG with standard magnetotransport experiments at 1.3 K using the Hall bar geometry of the sample with all gates grounded. The mobility of the 2DEG is $\mu = 1.04 \times 10^5$ cm^2/(Vs) and the electron density $n = 1.3 \times 10^{15}$ m^{-2}. Based on these numbers, we estimate the mean free path to be $l_e = 620$ nm, which is larger than the split-gate separation and the lithographic channel length of 500 nm.
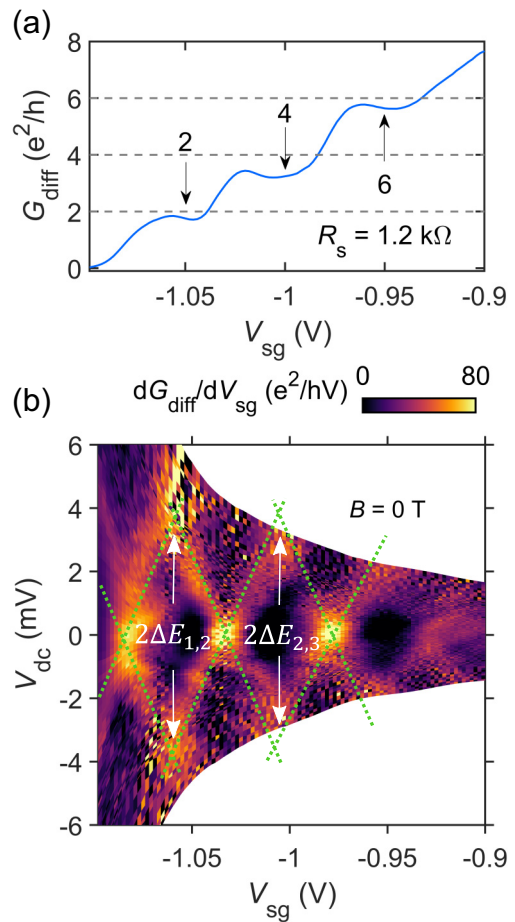

FIG. 2. (a) Differential conductance G_{diff} as a function of V_{sg} at a temperature of $T = 1.3$ K when no magnetic field is applied. Steps of the conductance are visible. A series resistance $R_s = 1.2$ kΩ has been subtracted. $G_{diff} = 2e^2/h$, $4e^2/h$, and $6e^2/h$ are labeled with dashed lines. (b) Finite bias spectroscopy showing the transconductance dG_{diff}/dV_{sg} as a function of V_{sg} and V_{dc}. A correction on the voltage drop through the quantum point contact (QPC) is made with $R_s = 1.2$ kΩ. The green dashed lines are added as guidance.

The transport measurement of the QPC uses standard low frequency (5 Hz) lock-in techniques together with a direct current (dc) measurement in a He^4 cryostat with a base temperature of 1.3 K. The same dc bias V_{sg} is applied to both parts of the split-gate to form the QPC in the 2DEG. We apply a fixed alternating current (ac) bias of $V_{ac} = 350\,\mu$V and a variable dc bias V_{bias} between contacts 1 and 4 and measure the ac and dc components of the two-terminal current I_{ac} and I_{dc}. In addition, we measure the ac and dc parts of the diagonal voltage-drop $V_{36,ac}$ and $V_{36,dc}$ between contacts 3 and 6. A rotatable magnetic field B can be applied in our experiment, where the angle between the direction of the magnetic field and the sample normal can be precisely calibrated with the Hall measurement. As shown in Fig. 1(b), we denote the magnetic field applied perpendicular to the sample surface as $B_\perp$ and the magnetic field aligned parallel to the sample surface but perpendicular to the current as $B_\parallel$.

The QPC is created by applying a negative V_{sg}. A special sweeping protocol is adopted for the gate voltages to achieve reproducible measurement results. The 1D channel can be pinched off completely by a sufficiently negative split-gate voltage. However, due to a time-dependent shift of the gate voltage characteristic in our Si-doped InSb/InAlSb heterostructures, the pinch-off lasts <1 min in our measurement. This short timescale does not allow us to perform successive conductance measurements for different source-drain voltages or magnetic fields. We, therefore, loop the gate voltage V_{sg} continuously between two carefully chosen bounds and thereby achieve reproducible gate characteristics that are stable in time. For all the measurements shown below, the protocol for sweeping V_{sg} is as follows: we measure the first V_{sg}-dependent conductance trace from zero voltage to channel pinch-off. Without any delay, we then tune V_{sg} back to zero and keep it there for >5 min. The next traces are obtained by repeating this
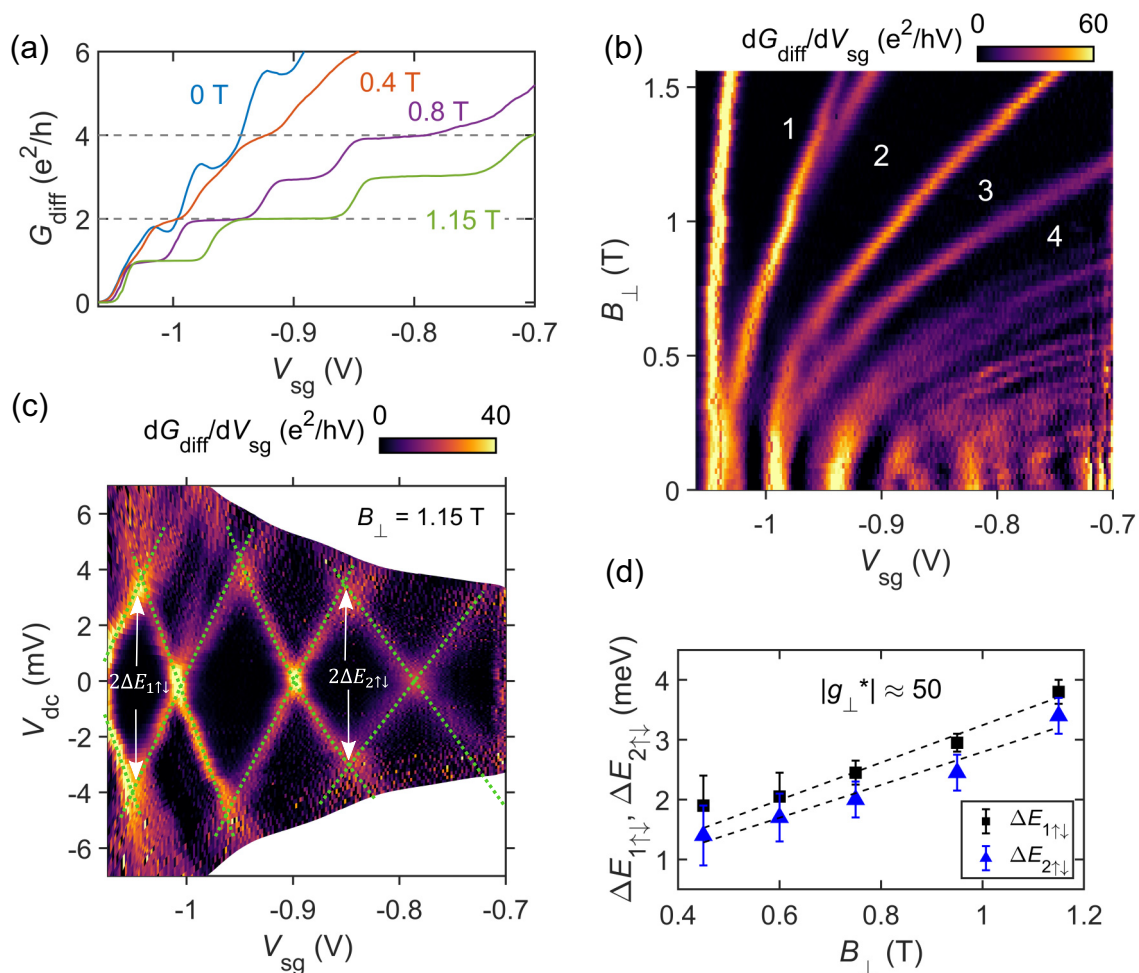

FIG. 3. (a) Differential conductance as a function of both $B_\perp$ and V_{sg}. The plateaus move to the correct value with the increase of $B_\perp$, and spin-split conductance plateaus are observable. A series resistance $R_s = 1.2\,$kΩ has been subtracted. $G_{diff} = 2e^2/h$ and $4e^2/h$ are labeled with dashed lines. (b) Transconductance dG_{diff}/dV_{sg} as a function of $B_\perp$ and V_{sg}. Both magnetic depopulation and spin splitting are visible. In different dark regions, the corresponding values of the conductance are labeled in the unit of e^2/h. (c) Finite bias spectroscopy showing the transconductance dG_{diff}/dV_{sg} as a function of V_{sg} and V_{dc} when $B_\perp = 1.15$ T. The green dashed lines are added as guidance. (d) With a series reproduction of measurement in (c), the $B_\perp$ dependence of $\Delta E_{1\uparrow\downarrow}$ and $\Delta E_{2\uparrow\downarrow}$ is obtained. The error bars are determined by observing the height of the transconductance peaks in the cuts in the V_{sg} direction. The linear fit shows the out-of-plane g factor with a value of $|g_\perp^*| \approx 50$.

procedure. We find that different sweep rates and different resting times at $V_{sg} = 0$ can change the V_{sg} required to pinch off the channel. Therefore, all the measurements shown below are performed with the same measurement protocol within one cooldown with a total measurement time of 3 wk.

Figure 2(a) presents the differential conductance $G_{diff} = I_{ac}/V_{36,ac}$ as a function of V_{sg} when $V_{bias} = 0$. A constant series resistance $R_s = 1.2\,k\Omega$ is subtracted. In the later experiment, R_s is always kept at $1.2\,k\Omega$, assuming that the variation of the magnetoresistance is negligible in the range of B where the measurement is performed. With decreasing V_{sg}, the channel gradually gets pinched off, and conductance steps that correspond to 6, 4, and 2 conductance quanta can be observed. The absolute heights of these steps are always lower than the correct values, possibly because of backscattering, and the curve is more oscillatory than for a standard QPC in GaAs heterostructures.

In the next step, we perform finite bias spectroscopy by applying a nonzero V_{bias} to measure the mode spacing of the QPC. With the measurement protocol introduced above, we measure the V_{sg} dependence of the conductance and step V_{bias} after each such sweep while V_{sg} is zero. This is different from the commonly used way in which V_{bias} is swept and V_{sg} is stepped. Here, we subtract the voltage drop across R_s from $V_{36,dc}$ to obtain V_{dc}, i.e., $V_{dc} = V_{36,dc} - I_{dc} \times R_s$. Figure 2(b) depicts the differential transconductance dG_{diff}/dV_{sg} of the QPC as a function of both V_{sg} and V_{dc}. The dark regions in the colormap represent conductance plateaus; the light regions mark the transition between them. The extent in V_{dc} of the diamondlike plateau regions measures the energy separation of the QPC modes. We read the mode spacing using the auxiliary green dotted lines in the figure and find values $\Delta E_{1,2} \approx 3.8$ meV and $\Delta E_{2,3} \approx 3.5$ meV. In a harmonic potential approximation, this mode spacing is related to the frequency ω_0 via $\Delta E_{i,i+1} = \hbar\omega_0$. The real-space extents of the modes L_n with $n = 1$ and 2 are then calculated according to $\frac{m^*}{2}\omega_0^2 L_n^2 = \hbar\omega_0(n-\frac{1}{2})$. Here, we use the electron effective mass $m^* = 0.017m_e$, where m_e is the free electron mass. This value has been obtained through the temperature dependence of Shubnikov–de Haas oscillations in our previous paper on InSb QWs with the same thickness [34]. We find $L_1 \approx 34$ nm and $L_2 \approx 64$ nm, as expected, smaller than the separation of the split gates.

In the following, we investigate the effect of $B_\perp$ on transport through the QPC. In Fig. 3(a), the dependence of G_{diff} on V_{sg} for different $B_\perp$ is presented. With increasing $B_\perp$, the absolute heights of the conductance plateaus gradually move to the expected quantized values, and the steplike features become more pronounced. This is because the applied $B_\perp$ reduces backscattering through the channel. Due to the Zeeman effect, the two spin-degenerate states in each mode start to separate, and the plateaus at odd multiples of the quantum conductance become observable. The transconductance dG_{diff}/dV_{sg} is presented as a function of $B_\perp$ and V_{sg} in Fig. 3(b). For increasing $B_\perp$, the bright lines, which indicate the transitions between conductance plateaus, curve toward higher gate voltages, an effect known as the magnetic depopulation of QPC modes. They tend to approach a linear slope as they gradually merge
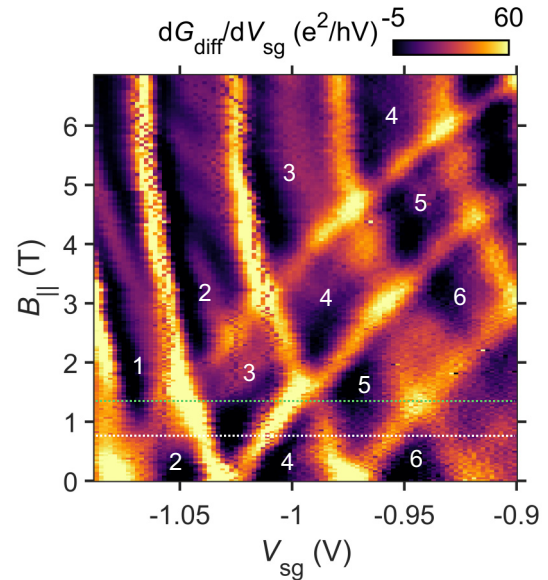

FIG. 4. Transconductance dG_{diff}/dV_{sg} as a function of $B_\parallel$ and V_{sg}. The spin-degenerated conductance plateaus split according to the Zeeman effect and are labeled with the associated conductance in the unit of e^2/h.

into the Landau levels which form at high magnetic fields. The magnitude of the Zeeman energy can be mapped by finite bias measurement with a nonzero $B_\perp$ applied. Figure 3(c) shows the transconductance dG_{diff}/dV_{sg} vs V_{dc} and V_{sg} at $B_\perp = 1.15$ T. The extent in V_{dc} direction of the first and the third diamonds corresponds to the Zeeman energy $\Delta E_{1\uparrow\downarrow}$ and $\Delta E_{2\uparrow\downarrow}$ between the spin-polarized states where $n = 1$ and 2, respectively. As presented in Fig. 3(d), by repeating the finite bias measurement with different $B_\perp$, we can estimate the out-of-plane effective g factor $g_\perp^*$ to have the value $|g_\perp^*| \approx 50$ with an uncertainty of about 10%, by linearly fitting $\Delta E_{1\uparrow\downarrow}$ and $\Delta E_{2\uparrow\downarrow}$ vs $B_\perp$.

In addition, we rotate the sample to have the magnetic field $B_\parallel$ applied in plane, but perpendicular to the current. Figure 4 shows the transconductance dG_{diff}/dV_{sg} as a function of V_{sg} and $B_\parallel$. Each spin-degenerate state which contributes a conductance of $2e^2/h$ at zero field gradually splits into two spin-polarized states with increasing $B_\parallel$. As shown in Fig. 5(a), which is a cut of Fig. 4 at $B_\parallel = 0.75$ T (white dashed line), conductance plateaus with both even and odd multiples of the conductance e^2/h are visible. This is verified in the transconductance curve and the finite bias measurement presented in Fig. 5(b), where the number of the transconductance minima in the given range of V_{sg} doubles as compared with zero field. Increasing $B_\parallel$ in the range 1.3 T $< B_\parallel <$ 1.9 T in Fig. 4, we can tune the energy separation of two spin-polarized states in one subband to be about equal to the zero-field subband separation. For instance, as presented in Fig. 5(c), which is a cut along at $B_\parallel = 1.32$ T in Fig. 4 (green dashed line), the conductance plateaus now occur at odd multiples of e^2/h only. This is also seen in the transconductance trace and the finite bias measurement shown in Fig. 5(d), where the mode spacing is close to its zero-field value. Increasing $B_\parallel$ further, the Zeeman energy increases continuously. This
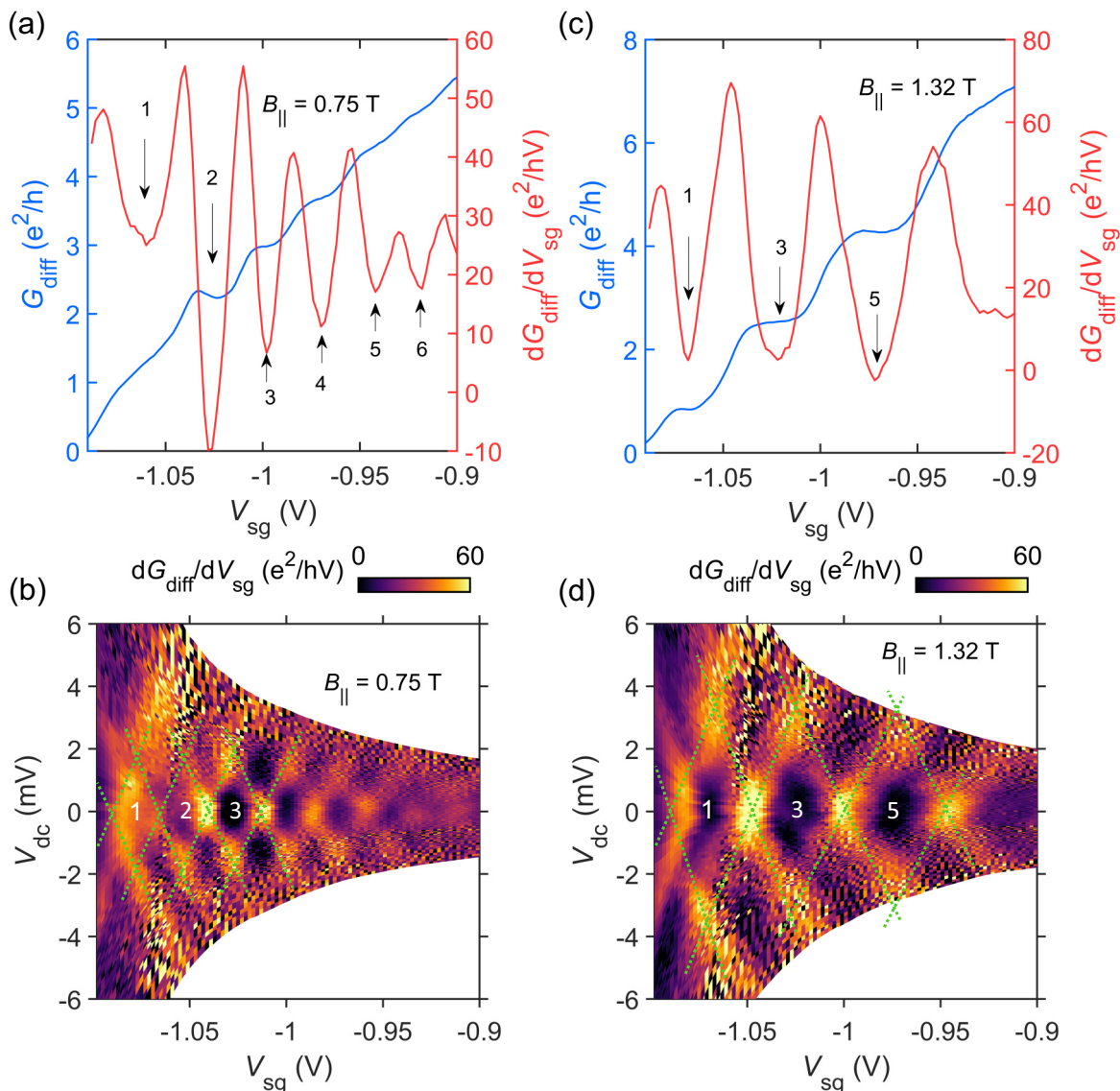
FIG. 5. (a) and (c) The V_{sg} dependence of the differential conductance G_{diff} and transconductance dG_{diff}/dV_{sg} when in-plane magnetic fields $B_{\parallel} = 0.75$ and 1.32 T are applied, respectively. The conductance plateaus are labeled in units of e^2/h. (a) and (c) are the cuts of Fig. 4 along the white and green dashed line, respectively. (b) and (d) are finite bias spectroscopy showing the transconductance dG_{diff}/dV_{sg} as a function of V_{sg} and V_{dc} with $B_{\parallel} = 0.75$ and 1.32 T applied, respectively. Green dashed lines are guidance.

leads to a pattern of closing and reopening gaps between neighboring spin-polarized states in Fig. 4, as indicated by the numbers.

The in-plane effective g factor $|g_{\parallel}^*|$ can be estimated by combining the measurements performed with $B_{\parallel}$ applied. There are two important features to be noticed. First, the lever arm of the split gate, relating a change of V_{sg} to a shift in mode energy, is nearly constant when $V_{sg} < -1$ V. This is found from the similarity of the slopes of the green dotted lines in Figs. 5(b) and 5(d). Second, in the same figures, the green dotted lines with the same direction are nearly parallel. These two observations indicate that the subband spacing $\Delta E_{1,2}$ is independent of $B_{\parallel}$. We examine the height of the transconductance peak around $V_{sg} = -1.05$ V by cutting Fig. 4 horizontally at different values of $B_{\parallel}$. We find that the Zeeman energy most closely equals the energy separation between the modes with

$n = 1$ and 2 when $B_{\parallel} = 1.65$ T, i.e.,

$$|g_{\parallel}^*| \, \mu_B B_{\parallel}|_{B_{\parallel}=1.65 \text{ T}} = \Delta E_{1,2},$$

where μ_B is the Bohr magneton. With the value $\Delta E_{1,2} \approx 3.8$ meV extracted from Fig. 2(b), we estimate the in-plane effective g factor to be $|g_{\parallel}^*| \approx 40$ with an uncertainty of about 10%, which is lower than $|g_{\perp}^*|$ found before. Alternatively, $|g_{\parallel}^*|$ can be extracted from the finite bias measurement presented in Fig. 5(b). Like the situation where only $B_{\perp}$ is applied, the extent of the diamonds with conductance e^2/h and $3e^2/h$ in V_{dc} direction corresponds to the Zeeman energy when $B_{\parallel} = 0.75$ T, where the Zeeman energy is observable but still $<\Delta E_{1,2}$. Thus, we can write $|g_{\parallel}^*| \, \mu_B B_{\parallel} = \Delta E_{1\uparrow\downarrow}$ and $|g_{\parallel}^*| \, \mu_B B_{\parallel} = \Delta E_{2\uparrow\downarrow}$. With the measurement showing $\Delta E_{1\uparrow\downarrow} \approx \Delta E_{2\uparrow\downarrow} \approx 1.8$ meV, we estimate $|g_{\parallel}^*| \approx 41$. Due to limited data quality,

this estimation may have a larger error than the estimate obtained from the zero bias measurement shown in Fig. 4. Furthermore, there may be larger errors in the estimation of $|g_\parallel^*|$ than that of $|g_\perp^*|$ because the parallel magnetic field does not reduce backscattering.

We now discuss our measurement results in the light of previous publications. Our device delivered a better data quality than the gate-defined device presented in Ref. [26]. Comparing our results with devices defined by etching, we find a slightly lower anisotropy of the effective g even though experimental uncertainties are significant. In Refs. [26,27] defined by chemical etching, the in-plane effective g factor was found to be about half of the out-of-plane effective g factor. In Ref. [26], the in-plane g factor is ∼26, but the out-of-plane g factor is ∼52. Similarly, in Ref. [27], the in-plane g factor is ∼40, while the out-of-plane g factor is ∼60. The lower g factor anisotropy in our device may be related to a weaker SOI in our system. Because the Si doping is incorporated almost symmetrically around the QW in our device, we expect the wavefunction of electrons to sit more symmetrically in the QW than in previous papers. Therefore, the Rashba contribution to the SOI is likely to be smaller in our system. Because of the huge effective g factor in the bulk, the Zeeman energy can exceed the contribution of the Dresselhaus SOI at a relatively small magnetic field. In agreement with that, within our measurement precision, a smaller g factor anisotropy is observed. As a result of the insignificant SOI and the data quality limitation, we did not find signatures of avoided-crossing effects of the levels either. The tendency that the out-of-plane g factor is larger than the in-plane g factor is in accordance with the calculation in Ref. [36], but both g factors should not exceed the g factor in the bulk if only the $\mathbf{k} \cdot \mathbf{p}$ model is adopted. In our device, the value $|g_\perp^*| \approx 50$ is close to the g factor in the bulk but much larger than the value obtained from the coincidence measurement. A detailed introduction of the coincidence measurement and the $\mathbf{k} \cdot \mathbf{p}$ theory calculation can be found in Refs. [30,31,34]. Especially, in Ref. [34], the g factor of an InSb QW with the same thickness shows a value of $|g^*| = 35$, and it meets the $\mathbf{k} \cdot \mathbf{p}$ theory result, when an increased bandgap due to the QW confinement is considered. We were able to reproduce this coincidence measurement result with the Hall bar of the QPC device presented in this paper, finding the g factor to be between 35 and 40. Furthermore, we find that there is no obvious g factor enhancement due to electron-electron interactions. Beyond the comparison with QWs, the effective g factor that we obtained from the QPC measurements may be compared with g factor measurements in QPCs based on InSb nanowires. Although in most of the publications [18,19], the effective g factor is found to be ∼40 because of the confinement, it is possible that the effective g factor is enhanced in these devices due to electron-electron interactions in the constriction, where the carrier density is low [17]. However, since there is no observable signature related to strong electron-electron interactions, such as the 0.7 e^2/h anomaly, this interpretation still needs more support by investigating QPCs with higher quality.

In conclusion, we presented a completely gate-defined QPC device based on a 2DEG in an InSb QW. With a special gate operation protocol, the device maintains dynamical electrostatic stability. The energy separations between the QPC modes are determined using finite bias measurements. Spin-resolved transport through the nanostructure is observed in both in-plane and out-of-plane magnetic field. The value of the effective g factor is ∼50 for the magnetic field applied normal to the plane and ∼40 with the field applied in plane. The out-of-plane g factor is larger than the value obtained from the 2DEG using the coincidence method in the same device and larger than the value estimated from $\mathbf{k} \cdot \mathbf{p}$ theory. The unusual but necessary measurement protocol limits the further development of InSb nanodevices because of the long measurement time and the challenge of integrating more gates. Therefore, the problem of time-dependent gate characteristics needs to be solved before further progress can be made. We expect that more optimization of the heterostructure growth will provide enhanced device stability, which may pave the way for more elaborate nanostructures based on InSb QWs.

[1] O. Madelung, U. Roessler, and M. Schulz, *Landolt-Bernstein-Group III Condensed Matter* (Springer, Berlin, 2000), Vol. 41D.

[2] R. L. Kallaher, J. J. Heremans, N. Goel, S. J. Chung, and M. B. Santos, Spin-orbit interaction determined by antilocalization in an InSb quantum well, Phys. Rev. B **81**, 075303 (2010).

[3] G. A. Khodaparast, R. E. Doezema, S. J. Chung, K. J. Goldammer, and M. B. Santos, Spectroscopy of Rashba spin splitting in InSb quantum wells, Phys. Rev. B **70**, 155322 (2004).

[4] M. A. Leontiadou, K. L. Litvinenko, A. M. Gilbertson, C. R. Pidgeon, W. R. Branford, L. F. Cohen, M. Fearn, T. Ashley, M. T. Emeny, B. N. Murdin, and S. K. Clowes, Experimental determination of the Rashba coefficient in InSb/InAlSb quantum wells at zero magnetic field and el-evated temperatures, J. Phys. Condens. Matter **23**, 035801 (2011).

[5] A. M. Gilbertson, W. R. Branford, M. Fearn, L. Buckle, P. D. Buckle, T. Ashley, and L. F. Cohen, Zero-field spin splitting and spin-dependent broadening in high-mobility InSb/In$_{1-x}$Al$_x$Sb asymmetric quantum well heterostructures, Phys. Rev. B **79**, 235333 (2009).

[6] T. Ashley, A. Dean, C. Elliott, G. Pryce, A. Johnson, and H. Willis, Uncooled high-speed InSb field-effect transistors, Appl. Phys. Lett. **66**, 481 (1995).

[7] H. Chen, J. Heremans, J. Peters, A. Govorov, N. Goel, S. Chung, and M. Santos, Spin-polarized reflection in a two-dimensional electron system, Appl. Phys. Lett. **86**, 032113 (2005).

[8] I. Zutic, J. Fabian, and S. D. Sarma, Spintronics: Fundamentals and applications, Rev. Mod. Phys. **76**, 323 (2004).

[9] V. Mourik, K. Zuo, S. M. Frolov, S. R. Plissard, E. P. A. M. Bakkers, and L. P. Kouwenhoven, Signatures of Majorana fermions in hybrid superconductor-semiconductor nanowire devices, Science **336**, 1003 (2012).

[10] Y. Oreg, G. Refael, and F. von Oppen, Helical Liquids and Majorana Bound States in Quantum Wires, Phys. Rev. Lett. **105**, 177002 (2010).

[11] C. T. Ke, C. M. Moehle, F. K. de Vries, C. Thomas, S. Metti, C. R. Guinn, R. Kallaher, G. Lodari, G. Scappucci, T. Wang, R. E. Diaz, G. C. Gardner, M. J. Manfra, and S. Goswami, Ballistic superconductivity and tunable π-junctions in InSb quantum wells, Nat. Commun. **10**, 3764 (2019).

[12] A. Fornieri, A. M. Whiticar, F. Setiawan, E. Portolés, A. C. C. Drachmann, A. Keselman, S. Gronin, C. Thomas, T. Wang, R. Kallaher, G. C. Gardner, E. Berg, M. J. Manfra, A. Stern, C. M. Marcus, and F. Nichele, Evidence of topological superconductivity in planar Josephson junctions, Nature **569**, 89 (2019).

[13] S. Vaitiekėnas, G. W. Winkler, B. van Heck, T. Karzig, M.-T. Deng, K. Flensberg, L. I. Glazman, C. Nayak, P. Krogstrup, R. M. Lutchyn, and C. M. Marcus, Flux-induced topological superconductivity in full-shell nanowires, Science **367**, eaav3392, (2020).

[14] D. A. Wharam, T. J. Thornton, R. Newbury, M. Pepper, H. Ahmed, J. E. F. Frost, D. G. Hasko, D. C. Peacock, D. A. Ritchie, and G. A. C. Jones, One-dimensional transport and the quantisation of the ballistic resistance, J. Phys. C: Solid State Phys. **21**, L209 (1988).

[15] B. J. van Wees, H. van Houten, C. W. J. Beenakker, J. G. Williamson, L. P. Kouwenhoven, D. van der Marel, and C. T. Foxon, Quantized Conductance of Point Contacts in a Two-Dimensional Electron Gas, Phys. Rev. Lett. **60**, 848, (1988).

[16] T. Ihn, *Semiconductor Nanostructures: Quantum States and Electronic Transport*, (Oxford University Press, Oxford, 2010).

[17] I. van Weperen, S. R. Plissard, E. P. A. M. Bakkers, S. M. Frolov, and L. P. Kouwenhoven, Quantized conductance in an InSb nanowire, Nano Lett. **13**, 387 (2013).

[18] J. Kammhuber, M. C. Cassidy, F. Pei, M. P. Nowak, A. Vuik, Ö. Gül, D. Car, S. R. Plissard, E. P. A. M. Bakkers, M. Wimmer, and L. P. Kouwenhoven Conductance through a helical state in an Indium antimonide nanowire, Nat. Commun. **8**, 478 (2017).

[19] J. Kammhuber, M. C. Cassidy, H. Zhang, Ö. Gül, F. Pei, M. W. A. de Moor, B. Nijholt, K. Watanabe, T. Taniguchi, D. Car, S. R. Plissard, E. P. A. M. Bakkers, and and. P. Kouwenhoven, Conductance quantization at zero magnetic field in InSb nanowires, Nano Lett. **16**, 3482 (2016).

[20] J. C. E. Saldaña, Y. Niquet, J. Cleuziou, E. J. H. Lee, D. Car, S. R. Plissard, E. P. A. M. Bakkers, and S. De Franceschi, Split-Channel ballistic transport in an InSb nanowire, Nano Lett. **18**, 2282 (2018).

[21] M. de la Mata, R. Leturcq, S. R. Plissard, C. Rolland, C. Magén, J. Arbiol, and P. Caroff, Twin-Induced InSb nanosails: A convenient high mobility quantum system, Nano Lett. **16**, 825 (2016).

[22] S. T. Gill, J. Damasco, D. Car, E. P. A. M. Bakkers, and N. Mason, Hybrid superconductor-quantum point contact devices using InSb nanowires, Appl. Phys. Lett. **109**, 233502 (2016).

[23] E. M. T. Fadaly, H. Zhang, S. Conesa-Boj, D. Car, Ö. Gül, S. R. Plissard, R. L. M. Op het Veld, S. Kölling, L. P. Kouwenhoven, and E. P. A. M. Bakkers, Observation of conductance quantization in InSb nanowire networks, Nano Lett. **17**, 6511 (2017).

[24] N. Goel, J. Graham, J. C. Keay, K. Suzuki, S. Miyashita, M. B. Santos, and Y. Hirayama, Ballistic transport in InSb mesoscopic structures, Physica E **26**, 455 (2005).

[25] A. R. Dedigama, D. Deen, S. Q. Murphy, N. Goel, J. C. Keay, M. B. Santos, K. Suzuki, S. Miyashita, and Y. Hirayama, Current focusing in InSb heterostructures, Physica E **34**, 647 (2006).

[26] F. Qu, J. van Veen, F. K. de Vries, A. J. Beukman, M. Wimmer, W. Yi, A. A. Kiselev, B.-M. Nguyen, M. Sokolich, M. J. Manfra, F. Nichele, C. M. Marcus, and L. P. Kouwenhoven, Quantized conductance and large *g*-factor anisotropy in InSb quantum point contacts, Nano Lett. **16**, 7509 (2016).

[27] T. Masuda, K. Sekine, K. Nagase, K. S. Wickramasinghe, T. D. Mishima, M. B. Santos, and Y. Hirayama, Transport characteristics of InSb trench-type in-plane gate quantum point contact, Appl. Phys. Lett. **112**, 192103 (2018).

[28] W. Yi, A. A. Kiselev, J. Thorp, R. Noah, B. M. Nguyen, S. Bui, R. D. Rajavel, T. Hussain, M. F. Gyure, P. Kratz, Q. Qian, M. J. Manfra, V. S. Pribiag, L. P. Kouwenhoven, C. M. Marcus, and M. Sokolich Gate-tunable high mobility remote-doped InSb/In$_{1-x}$Al$_x$Sb quantum well heterostructures, Appl. Phys. Lett. **106**, 142103 (2015).

[29] C. A. Lehner, T. Tschirky, T. Ihn, W. Dietsche, J. Keller, S. Fält, and W. Wegscheider, Limiting scattering processes in high-mobility InSb quantum wells grown on GaSb buffer systems, Phys. Rev. Mater. **2**, 054601 (2018).

[30] B. Nedniyom, R. J. Nicholas, M. T. Emeny, L. Buckle, A. M. Gilbertson, P. D. Buckle, and T. Ashley, Giant enhanced *g*-factors in an InSb two-dimensional gas, Phys. Rev. B **80**, 125328 (2009).

[31] K. F. Yang, H. W. Liu, T. D. Mishima, M. B. Santos, K. Nagase, and Y. Hirayama, Nonlinear magnetic field dependence of spin polarization in high-density two-dimensional electron systems, New J. Phys. **13**, 083010 (2011).

[32] J. C. Chokomakoua, N. Goel, S. J. Chung, M. B. Santos, J. L. Hicks, M. B. Johnson, and S. Q. Murphy, Ising quantum Hall ferromagnetism in InSb-based two-dimensional electronic systems, Phys. Rev. B **69**, 235315 (2004).

[33] Z. Lei, C. A. Lehner, E. Cheah, M. Karalic, C. Mittag, L. Alt, J. Scharnetzky, W. Wegscheider, T. Ihn, and K. Ensslin, Quantum transport in high-quality shallow InSb quantum wells, Appl. Phys. Lett. **115**, 012101 (2019).

[34] Z. Lei, C. A. Lehner, K. Rubi, E. Cheah, M. Karalic, C. Mittag, L. Alt, J. Scharnetzky, P. Märki, U. Zeitler, W. Wegscheider, T. Ihn, and K. Ensslin, Electronic *g* factor and magnetotransport in InSb quantum wells, Phys. Rev. Res. **2**, 033213 (2020).

[35] I. Kulesh, C. Ting Ke, C. Thomas, S. Karwal, C. M. Moehle, S. Metti, R. Kallaher, G. C. Gardner, M. J. Manfra, and S. Goswami, Quantum Dots in an InSb Two-Dimensional Electron Gas, Phys. Rev. Appl. **13**, 041003(R) (2020).

[36] R. Winkler, *Spin Orbit Coupling Effect in Two Dimensional Electron and Hole Systems* (Springer, Berlin, Heidelberg, 2003).